

# Effects-Based Monitoring of Geomagnetically-Induced Current Using a Convolutional Neural Network

Adedasola A. Ademola<sup>1</sup>, Student Member, IEEE, Xiawen Li, Member, IEEE, Andrea Pinceti, Member, IEEE, Micah J. Till, Member, IEEE, Kevin D. Jones, Member, IEEE, R. Matthew Gardner, Senior Member, IEEE, and Yilu Liu<sup>2</sup>, Fellow, IEEE

**Abstract**—Geomagnetically-induced current (GIC) due to space weather can flow in the power grid causing undesirable effects such as transformer overheating, misoperation of protection devices, and potential blackouts. It is therefore important to monitor GIC in the power grid to improve online situational awareness and decision-making of system operators during a geomagnetic disturbance. To avoid the costly installation of GIC monitors at transformers' neutrals, it is desirable to find correlations between GIC and already-monitored parameters. Hence, this work proposed the use of a convolutional neural network (CNN) to compute GIC amplitudes from learned patterns in the time-series data of transformer even harmonic currents. Using an electromagnetic transient program, GIC injection simulations were performed for a modeled Dominion Energy Virginia (DEV) substation with two 504 MVA, 500/230 kV transformers. Data collected from these offline simulations were used to train the CNN to provide online GIC monitoring. Testing the CNN performance involved using real GIC measurements from published literature and from a physical GIC monitor in the DEV area. The results showed that the proposed method was able to provide GIC readings with a root mean squared error of 1.56 A/phase (equivalent to an average accuracy of 94%) for these real GIC waveforms.

**Index Terms**—Geomagnetically-induced current, geomagnetic disturbance, harmonics, machine learning, neural networks, power systems monitoring, reactive power consumption.

## I. INTRODUCTION

**L**ARGE expulsion of plasma and radiation from the sun in the form of coronal mass ejections and solar wind can

Manuscript received 22 December 2021; revised 8 April 2022; accepted 30 May 2022. Date of publication 8 June 2022; date of current version 24 January 2023. This work was primarily supported by Dominion Energy Virginia, Richmond, USA and supplemental support by the CURENT Industry Partnership Program and the ERC Program of the National Science Foundation and DOE under NSF Award EEC-1041877. Paper no. TPWRD-01910-2021. (Corresponding author: Adedasola A. Ademola.)

Adedasola A. Ademola is with the University of Tennessee, Knoxville, TN 37996 USA (e-mail: aademol1@vols.utk.edu).

Xiawen Li, Andrea Pinceti, Micah J. Till, Kevin D. Jones, and R. Matthew Gardner are with the Dominion Energy Virginia, Richmond, VA 23220 USA (e-mail: xiawen.li@dominionenergy.com; andrea.pinceti@dominionenergy.com; micah.j.till@dominionenergy.com; kevin.d.jones@dominionenergy.com; matthew.gardner@dominionenergy.com).

Yilu Liu is with the University of Tennessee, Knoxville, TN 37996 USA, and also with the Oak Ridge National Laboratory, Oak Ridge, TN 37830 USA (e-mail: liu@utk.edu).

Color versions of one or more figures in this article are available at <https://doi.org/10.1109/TPWRD.2022.3181250>.

Digital Object Identifier 10.1109/TPWRD.2022.3181250

cause geomagnetic disturbances (GMD) on the planet. GMD can induce geoelectric field on man-made conductors at the Earth's surface, e.g., communication lines [1], oil and gas pipelines [2], and electricity transmission lines [3]. The grounding of transmission lines by their connection with wye-connected transformers permits quasi-DC geomagnetically-induced current (GIC) to flow in the power grid. The principal source of GIC-related issues on the power grid is at the transformers, where GIC causes half-cycle saturation [4], which subsequently leads to transformer hotspot-heating, a significant increase in reactive power consumption, and generation of even and odd harmonics. The potential consequences of these GIC effects include permanent transformer damage, abnormal voltage levels, misoperation of protection devices, generator overheating, etc. [5], [6]. Combinations of these consequences have led to infamous events such as the system collapse of the Hydro Quebec system in Canada where 6 million people lost electricity for 9 hours [7]; and the blackout in Malmo, Sweden which put 50 thousand people in darkness for 1 hour [8]. GIC-related events have also been reported in the USA [9], South Africa [10], and New Zealand [11], among others. Apart from solar activities, GIC flow can also be caused by high-altitude nuclear electromagnetic pulse if a nuclear bomb is detonated at altitudes higher than 30 km above the earth's surface. Unsurprisingly, academia and industry have been seeking improved methods to monitor GIC in the grid so as to aid situational awareness during a GMD event. Enhanced situational awareness will enable system operators to make better decisions for the mitigation of GMD impacts; such decisions may include derating transformers with high GIC, switching on fans/pumps to improve transformer cooling, activation of controllable neutral switching devices, controlled load shedding, etc. Reliable GIC monitoring can also facilitate automatic activation of neutral blocking devices to speedily block GIC during GMD events while allowing grounding protection during normal system operation [6], [12].

GIC monitoring methods can be broadly divided into measurement-based, model-based, and effects-based techniques [6]. The first involves the direct measurement of GIC at transformer neutrals typically with Hall effect current transducers [13]. These devices are highly accurate with low error up to  $\pm 0.6\%$  [14], but they require physical installations at

substations. Numerous deployments of these devices can lead to significant financial burdens on utilities in terms of purchasing, logistics, and labor costs, hence, installations remain limited to a few critical substations. On the other hand, the model-based methods involve geophysical modeling of the transmission grid to calculate effective GIC flow in lines and transformers [15]. These are analytical methods suitable for system-level monitoring, but their simplicity and accuracies depend on underlying assumptions in the modeling. For example, the assumption of uniform geoelectric field and Earth's conductivity simplifies the model and reduces its input requirement at the expense of lower accuracy [16], [17]. In contrast, consideration of non-uniformities improves accuracy but requires more complicated modeling and spatially granular data which are not always available [15]. The model-based methods can also integrate available GIC measurements to improve performance [15], [17], but will suffer the same limitations as the measurement-based method.

Effects-based methods attempt to quantify transformer GIC based on its correlation with the half-cycle saturation effects that it causes. These effects can be thermal (e.g., hotspot heating), mechanical (e.g., vibration), or electrical (e.g., harmonics and reactive power consumption). Among these, the electrical effects are the most frequently used because they are easy to simulate and can be quickly computed online from normally measured system parameters [18], [19]. The effects-based methods are potentially the easiest to deploy since they do not require the installation of new devices or the collection of often unavailable data. However, low-magnitude GIC detection is often difficult or impossible using this class of methods. The authors in [19] developed an effects-based monitor which exploited the linear relationship between GIC and the 2<sup>nd</sup> harmonic magnitude in transformer magnetizing current. The study reported that only GIC above 6.4 A/phase for a 280 MVA transformer could be detected; larger GIC amplitudes may be undetectable for a larger transformer. The lack of consideration for the transient, non-linear relationship between harmonics and GICs also limited GIC detection speed. An effects-based monitor proposed in [20] used wavelet transforms and machine learning (ML) classification to detect GIC from harmonics (up to the 50<sup>th</sup> order) in the secondary winding of a current transformer. This method involved complicated feature extraction and was not tested on real GIC signals. Moreover, the use of the ML algorithm as a classifier limited the practical resolution of the detected GIC amplitude.

A major challenge of the effects-based methods lies in the non-obvious instantaneous correlation between GIC and its effects, especially for low GIC amplitudes. Fig. 1 presents an example of a low-magnitude GIC signal injected into a transformer neutral. The resulting reactive power loss ( $\Delta Q$ ) and harmonic current do not peak at the same time as the injected GIC signal. This is mainly because transformer saturation is a function of the integral of the DC voltage at the terminal of the transformer's magnetic circuit, rather than a function of the instantaneous GIC amplitude [4], [21]. It is therefore difficult to capture the dependencies between GIC and its effects without using some time-series data.

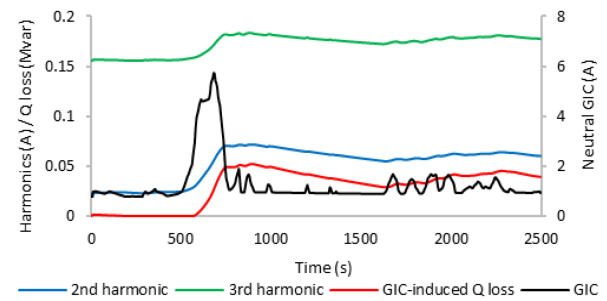


Fig. 1. Harmonics and Reactive power consumption due to GIC in transformer neutral.

Hence, this work developed an effects-based GIC monitoring method using a convolutional neural network (CNN) to recognize patterns in the time-series data of the harmonics generated due to GIC flow. CNNs are especially suitable for multivariate time-series data because it allows for multi-dimensional input shape. The convolution operation can be intuitively understood as a sliding window over the time series data of different input parameters. This allows the algorithm to automatically capture temporal changes in its inputs that are associated with specific outputs during training. CNNs are widely used for time-series problems due to their robustness and smaller amount of training time compared to more complex architectures like recurrent neural networks [22]–[24]. The use of CNN for online GIC monitoring in this work leverages offline electromagnetic transient with DC analysis (EMTDC) simulations which provide training and testing data for the CNN.

The rest of this paper is organized as follows. Section II highlights the offline simulations and feature extraction performed to create the dataset for the CNN training and testing. Section III elucidates the construction of the CNN along with its training. Section IV reports the performance of the proposed method, while conclusions are presented in Section V.

## II. CREATION OF DATASET FOR CNN TRAINING AND TESTING

### A. Substation Modelling in EMTDC/PSCAD

The transmission network of Dominion Energy Virginia (DEV) modeled in ASPEN OneLiner was reduced to its Thevenin equivalent model from the perspective of two substation buses as shown in Fig. 2. Bus 1 and 2 are 500 kV and 230 kV buses respectively. They are connected by two 504 MVA grounded wye-connected autotransformers, TX1 and TX2, both with single-phase bank core types. TX3 is a wye-wye connected virtual transformer that represents the network connections between the two buses external to the substation. G1 and G2 are virtual voltage sources that represent the network's equivalent boundary conditions at each bus.

The substation model was recreated in EMTDC/PSCAD using relevant data from ASPEN OneLiner such as voltage magnitudes and angles for the generators; transformer leakage reactances and copper losses; as well as positive and zero sequence impedances for the generators and transformers. The

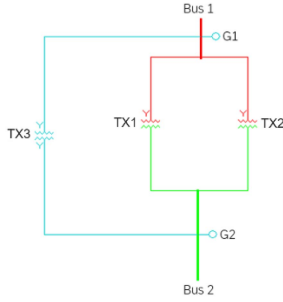


Fig. 2. Thevenin equivalent of Dominion Energy Virginia transmission grid from a substation's reference point.

TABLE I  
BOUNDARY CONDITIONS AT BUS 1 AND 2 FOR SELECTED TOPOLOGIES

	Topo-logy	Voltage (pu)	Positive Sequence Impedance (pu)	Zero Sequence Impedance (pu)
G1	N-0	$1.030 \angle 30.20$	$0.00021 + j0.0063$	$0.00130 + j0.0120$
	N-1	$1.034 \angle 30.00^0$	$0.00033 + j0.0098$	$0.00250 + j0.0200$
	N-2	$1.036 \angle 30.06^0$	$0.00039 + j0.0105$	$0.00245 + j0.0205$
G2	N-0	$0.980 \angle 30.60$	$0.00245 + j0.0200$	$0.00590 + j0.0200$
	N-1	$0.980 \angle 30.57^0$	$0.00240 + j0.0198$	$0.00550 + j0.0198$
	N-2	$0.98 \angle 30.60^0$	$0.00250 + j0.0202$	$0.00550 + j0.0198$

electromagnetic simulations in EMTDC/PSCAD are more accurate than other simulation techniques for GIC effects due to their full dynamic modeling and consideration of nonlinear magnetization effects [25].

To represent system conditions during normal operation (N-0) and under contingencies: N-1 and N-2, three separate models were created in EMTDC/PSCAD. The N-1 and N-2 topologies were created by tripping line(s) close to the substation buses that led to the greatest reduction in the fault current at Bus 1. Table I presents the system conditions for the three topologies showing the increased impedance of G1 at N-1 and N-2 topologies which indicate the reduced grid strength during these contingencies. Consideration of these contingency topologies allowed the CNN to capture harmonics level variations for different system impedances. Fault analysis was performed in PSCAD and ASPEN OneLiner to validate the three topology models. This involved the measurement of fault currents for three-phase-to-ground and line-to-line faults at Bus 1 and 2. The results showed that the absolute errors of the fault currents calculated in PSCAD were less than 1% relative to those calculated in the ASPEN model. Furthermore, the curve-fitting optimization method described in [26] was deployed to calculate the knee voltage and magnetizing current for TX1 and TX2, using the measured V-I data points of DEV's physical transformers. Air core reactances for the two transformers were estimated as twice the transformer leakage reactance [27].

### B. GIC Injection Simulations

GIC flow in the transformer was simulated by injecting DC into the transformers' neutrals from DC voltage sources connected to them. Assuming equal GIC flow in each phase,

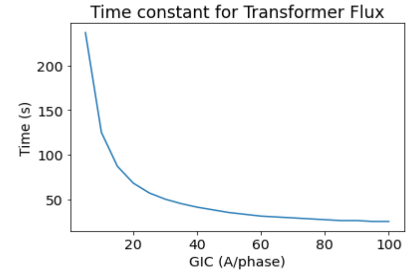


Fig. 3. Flattening of transformer flux time constant at higher GIC levels.

currents from the DC sources are 3 times the neutral GIC amplitudes in A/phase; this is a typical assumption made to simply calculations and allow one-line representation of the power system during a GMD event [28]. Neutral GIC amplitudes were controlled using a Proportional–Integral (PI) controller with a proportionality gain of 3 and an integral time constant of 0.1 s. The PI controller received its control signal from a connected signal generator with variable frequency, duty cycle, and magnitude. A virtual parallel RLC load was also connected at Bus 2 to allow for variation of the transformer loading. Real and reactive power are taken as the inputs of the virtual load which automatically calculates the equivalent RLC values. In practice, the appropriate load model to use will depend on the actual load composition that is downstream of the bus.

To create a dataset for CNN training, DC injection simulations were separately performed for the three models representing different network topologies. For each model, two categories of control signals were used to simulate GIC injection:

- i. DC signals
- ii. Square wave signals with 0.005 Hz frequency and 50% duty cycle

Along with DC signals, square waves are used by transformer manufacturers to calculate transformer GIC capability curves when information about a specific GIC waveform to use is limited [29]. These signals were similarly used in this work to represent GIC waveforms during CNN training when the specific trajectory of transformer GIC is unknown. The square waves' frequency was selected as a mid-point of the typical 0.0001 – 0.1 Hz frequency range of GIC [30]. The DC control signals were used to simulate constant-amplitude GIC of 0 A/phase; 2.5 A/phase; 5 – 50 A/phase in steps of 5 A; and 50 – 100 A/phase in steps of 10 A. These values also serve as the maximum amplitudes of the square wave control signals used to simulate oscillating GIC. The increasing interval size reduced the number of simulations performed since there is a decreasing difference in the transient effects of GIC at higher magnitudes. This can be seen in Fig. 3 where the time constant of transformer flux flattens at higher GIC amplitudes. 100 A/phase was the highest simulated GIC magnitude because the maximum expected GIC magnitude for a 1-in-100-year worst storm scenario in the DEV system is approximately 89 A/phase [19], [28].

Transformer loading was also varied by adjusting the active load of the virtual load at Bus 2 from 50 to 2150 MW in steps of 100 MW and 190 MW for simulations using DC and square wave control signals respectively. It was assumed that many

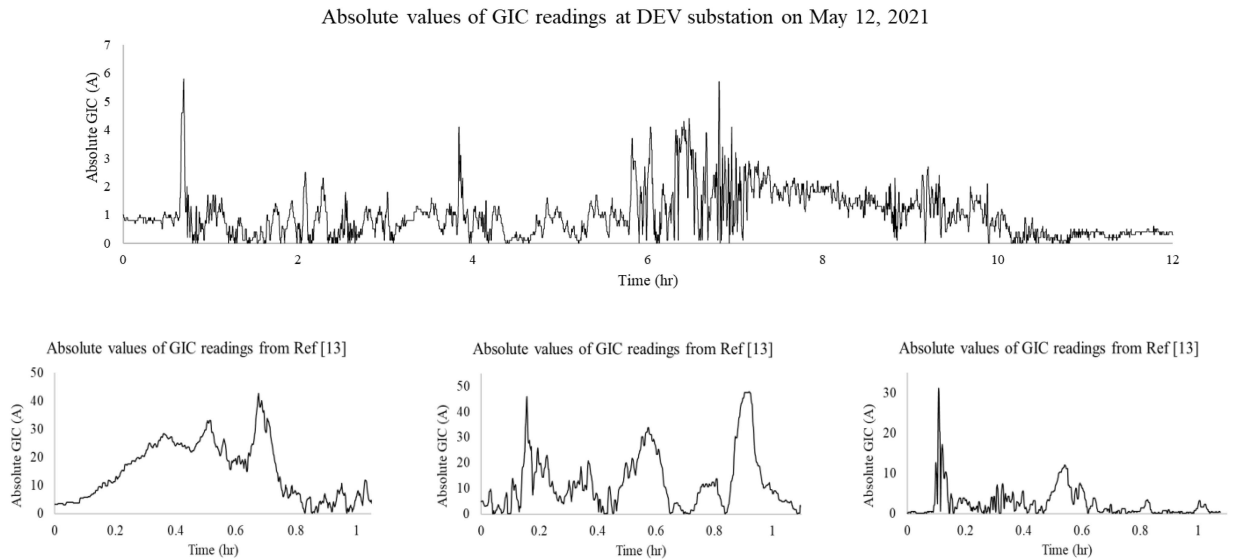


Fig. 4. GIC measurements collected from DEV GIC monitor (top) and published literature (bottom) to create the test dataset.

of the important dependencies between GIC and its effects would already be “learnable” by the neural network from the data extracted from the simulations with DC control signals. So, a smaller number of simulations with square wave control signals were required; this helped to reduce the total number of simulations performed. To control transformer reactive load, a PI controller was used to modulate the reactive power of the virtual load until desired transformer secondary side P:Q ratios were achieved. The desired P:Q ratios for a transformer load were chosen to represent typical values found in DEV’s 3-year operational data of the physical transformers. Run times for simulations with DC control signals were selected based on the GIC levels to allow transformer parameters to reach steady state. The run times range from 90 s for GIC amplitudes greater than 30 A/phase to 780 s for amplitudes less than 5 A/phase. For simulations with square wave control signals, run times were chosen to allow the waveform to complete 3 cycles, i.e., 600 s.

To create the test dataset, real measurements from a GIC monitor installed at the modeled DEV substation were used alongside other real GIC measurements published in [13]. In total, about 15 hours’ worth of GIC measurements were collected from the two sources. Their absolute values, shown in Fig. 4, were used since GIC has the same effects whether flowing in or out of a transformer [9]. The collected measurements were used to create 90 GIC signals by segmenting the 15-hour measurements into 10-minute blocks. To increase the variability and number of the GIC signals, each 10-minute block was scaled by a multiplier. The multiplier was calculated as the ratio of the peak amplitude of the 10-minute block to a randomly selected amplitude between 1 – 100 A/phase. In this way, 810 scaled GIC signals were created from the 90 extracted signals to simulate a variety of GIC injections for the 3 topology models. The signal generator used for the training dataset simulations was replaced by PSCAD’s playback module to inject the scaled GIC signals for the test dataset simulation. Transformer loading for the test

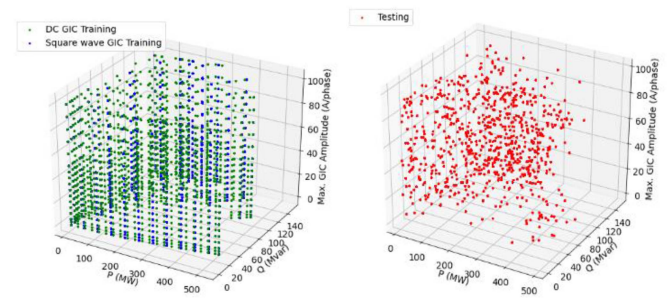


Fig. 5. Transformer load and GIC combinations that constitute the training (left) and testing (right) datasets.

dataset was also randomly selected within the transformer’s operating range. The randomized conditions in the test dataset were useful in evaluating the generalization capacity of the trained CNN. Fig. 5 presents the transformer loading and peak GIC amplitudes for the 5811 and 810 simulations that constitute the training and testing datasets respectively. PSCAD Fast Fourier Transform (FFT) modules were used to decompose the harmonic components ( $1^{\text{st}}$  –  $7^{\text{th}}$  order) of the primary and secondary side currents. After each simulation, per second RMS values of these harmonic components were saved for subsequent feature extraction. The simulations were implemented using the Python API for PSCAD, and simulations for each topology model were run concurrently using three instances of PSCAD workspace on an Intel Core i7-9700 CPU with 16 GB RAM. Total clock times to perform the simulations for the training and testing datasets were 95.6 and 17 hours respectively.

### C. Feature Extraction

In this work, the monitored effects used to compute GIC are the RMS values of the  $2^{\text{nd}}$ ,  $4^{\text{th}}$ , and  $6^{\text{th}}$  harmonics in the transformer primary and secondary-side currents. These transformer

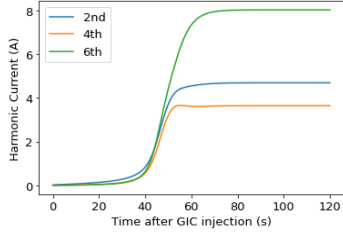


Fig. 6. Trajectories of the selected current harmonics due to GIC injection.

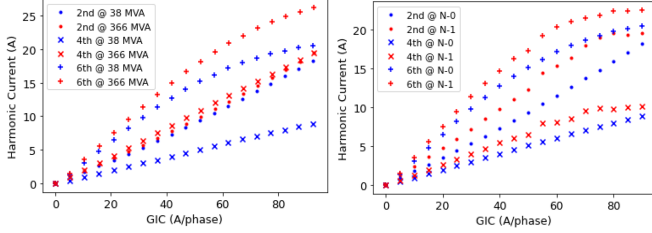


Fig. 7. Variation of steady-state values of current harmonics with GIC magnitudes, transformer loads (left), and network topologies (right).

currents are usually monitored in real-time for differential protection, so their use for the proposed method should not add financial or logistical costs for utilities. The selected harmonic orders were chosen because of their uniqueness to the half-cycle saturation of transformers under DC bias conditions. Typically, even harmonics are not found during the normal operation of power systems, so detection of the selected harmonic orders is a reliable indication of transformer half-cycle saturation due to GIC [31]. Since magnitude typically reduces at higher harmonic orders, we selected the three lower-order even harmonics for this work. Fig. 6 shows the selected harmonics in the secondary-side load current of transformer TX1 when a constant amplitude GIC of 25 A/phase is injected into its neutral. Transient and steady-state periods are clearly visible; the transient period can range from several seconds to several minutes depending on GIC amplitude and transformer loading [19]. Furthermore, current harmonics due to GIC are influenced by transformer loading and network topology especially at higher GIC amplitudes as shown in Fig. 7. Thus, fast GIC detection based on harmonic measurements requires the CNN to learn the transient and steady-state relationships between current harmonics, GIC magnitudes, transformer loading, and network topology.

Bearing these in mind, the features extracted from each simulation data include:

- Time-series data of transformer primary and secondary-side current harmonics ( $n$ -HV &  $n$ -LV, where  $n = 2, 4,$  and  $6$ ) using a 45 s window.
- Neutral GIC,  $I_{gic}$ , for the last second of each 45 s window.
- Transformer secondary-side real and reactive load,  $P$  and  $Q$ , at the last second of each 45 s window.
- Topology index,  $tp$ , to differentiate data for each topology model.

The features above were extracted to create the training and testing datasets with array shapes of  $(1220455 \times 274)$  and  $(451169 \times 274)$  respectively. Each sample of the arrays has 274

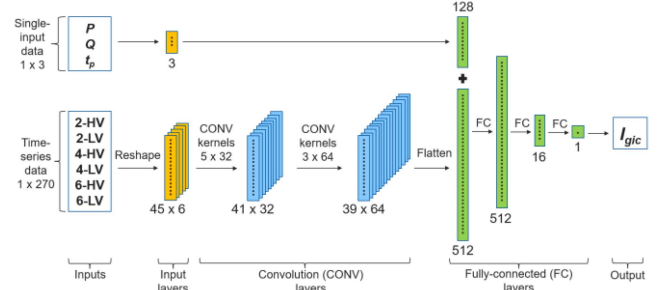


Fig. 8. Structure of the CNN for GIC monitoring.

values to represent conditions at a time,  $t$ . Values of the three harmonic orders in the primary and secondary currents from time  $t - 44$  to  $t$  make up 270 values ( $45 \cdot 3 \cdot 2 = 270$ ). The other 4 values are  $I_{gic}$ ,  $P$ ,  $Q$ , and  $tp$  at time  $t$ . In practice, there only needs to be a memory buffer to store the harmonic values from time  $t - 44$  to  $t - 1$ . The memory will be updated every second using a first-in-first-out method as new measurements become available.

### III. CONVOLUTIONAL NEURAL NETWORK (CNN)

#### A. CNN Structure and Training

CNNs are classes of artificial neural networks used to process data that have grid-like topology. Examples of such data include time-series data interpreted as a 1-D grid of samples at regular time intervals; and image data taken as a 2-D grid of pixel values. A CNN typically contains multiple hidden layers which are sparsely connected through groups of convolutional kernels. The kernels extract patterns from the input or previous layers through a cross-correlation operation that is similar to convolution operation without kernel flipping [32]. Using this operation, deeper CNN layers are able to capture and analyze more and more input patterns towards accurate recognition of the input. The effectiveness of CNNs is attributed to this hierarchical structure which was inspired by the human visual cortex system.

In this work, a CNN was used to identify patterns in the time-series data of the selected current harmonics ( $n$ -HV &  $n$ -LV) to detect GIC and compute its magnitude. Fig. 8 presents the structure of the CNN. To fit a single sample of  $n$ -HV and  $n$ -LV to the input of the CNN, it is reshaped to an array of shape  $(45 \times 6)$ , where each column represents the 45 s data of the selected current harmonics. On the other hand, single value inputs,  $P$ ,  $Q$ , and  $tp$ , are directly passed into a 128-node fully-connected (FC) layer that is concatenated with another FC layer.

This FC layer has 512 nodes and it receives the output of the two convolutional layers after they have been flattened. The kernels of the first convolutional layer have a  $(5 \times 32)$  shape, i.e., kernel size equals 5, and number of channels equals 32, while the second convolution layer has kernels with shape of  $(3 \times 64)$ . The convolution kernels perform the following operation on each of the inputs:

$$O(i, j) = \sigma \left( \sum_{u=0}^{kn-1} \sum_{v=0}^{ks-1} I(i+u, j+v) \cdot w(u, v) + b \right) \quad (1)$$

TABLE II  
CNN PERFORMANCE OVER TEST DATA

	Network Topologies			Total
	N-0	N-1	N-2	
RMSE over test data (A/phase)	1.55	1.57	1.56	1.56
ANZG over test data (%)	93.7%	94.4%	94.1%	94.1%

Where,  $I(u, v)$  is the input at position  $u$  of the  $v$ th channel of a convolutional layer;  $O(i, j)$  is the output at position  $i$  of the  $j$ th channel in the next convolutional layer;  $w(u, v)$  are kernel weights;  $b$  is kernel bias;  $\sigma(\cdot)$  is the activation function;  $ks$  and  $kn$  are kernel size and number of kernel channels respectively.

Hence, each convolutional layer output is the weighted sum of  $ks \times kn$  inputs from the previous layer, transformed by a non-linear activation function. All layers in the network employ the rectified linear units (ReLU) activation function, and their weight initialization was performed using the Kaiming initialization (HeNormal) method. Mean absolute error loss function and the adaptive moment estimation (Adam) optimizer were used to train the CNN. The learning rate was initially set to 0.00005 but was adaptively programmed to reduce by 50% if training error does not reduce over 10 training epochs. Other optimizer parameters were left at their default values. Furthermore, 5% of the training data was set aside to be used as validation data. The validation data was utilized to detect overfitting during training. So, training is automatically stopped when the CNN output error on the validation data stops reducing over 50 epochs. Using these training methods, the total training time for the CNN was approximately 1 hour, 25 mins on a computer with 16 GB Tesla P100 GPU.

#### IV. CNN PERFORMANCE EVALUATION

To evaluate the CNN performance for GIC monitoring, the root mean squared error (RMSE) was used since it retains measurement units and penalizes large deviations between the CNN output and true GIC values. However, RMSE gives no insight into the proportion of error relative to the true GIC values, e.g., a 3 A error is more significant for 5 A GIC amplitude than for 80 A GIC amplitude. Hence, another metric named accuracy over non-zero GIC (ANZG) was used to provide average accuracy relative to true GIC values while avoiding zero division issues as shown in Eq. 2.

$$ANZG = 1 - \frac{\sum_{s=1}^N \sum_t^{T_s} \frac{abs(I_{gic,true}(t) - I_{gic}(t))}{I_{gic,true}}}{NT_s} \quad (2)$$

for  $I_{gic,true} > 0$

Where  $I_{gic,true}(t)$  is the true injected GIC amplitude at time,  $t$ , for simulation,  $s$ .  $T_s$  is total simulation time equal to 600 s for the test simulations and  $N$  is total number of simulations in the test dataset.

##### A. CNN Performance Over Test Data

Table II presents the CNN performance for each topology in the test dataset. The low RMSE (and high ANZG) of the CNN output for real GIC signatures in the test dataset proves the

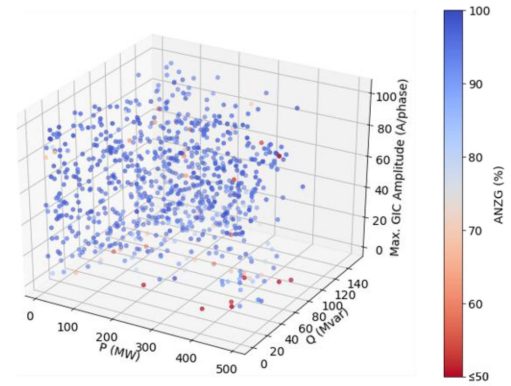


Fig. 9. ANZG for the simulations in the test dataset.

effectiveness of the proposed method for GIC monitoring. It also shows that the CNN can sufficiently generalize over unfamiliar transformer loading and different network topologies.

A plot of ANZG for each scenario in the test data set is shown in Fig. 9. Generally, average accuracies are well above 80%, but low accuracy is prevalent for GIC waveforms that have very low maximum amplitudes, especially when the transformer is heavily loaded. Low GIC amplitudes produce lower harmonic levels and high load typically dampens harmonics, thus, this combination of effects reasonably reduces the sensitivity of CNN. Fig. 10 presents visual comparisons between the CNN output and four 1-hour blocks of the curated GIC signals at different transformer loads and network topologies. These transformer loads are from actual measurements data of DEV's physical transformers. It can be seen that the CNN's output follows the trajectories of the GIC signals with high fidelity. The use of CNN as a regressor in this work allowed for higher GIC resolution compared to [20] which involved classification of detected GIC into discrete ranges.

Moreover, the overall average accuracy of 94.1% achieved in this work for waveforms based on real GIC measurements is superior to the highest accuracy of 90.95% reported for the classifier in [20]. The first plot in Fig. 10 further shows that the CNN can detect GIC levels as low as 1 A/phase. In fact, CNN accuracy for GIC above 1 A/phase is 96.5%, but accuracy for GIC below 1 A/phase is 22.1%. Thus, 1 A/phase is the lower detection threshold for the proposed method. This is less than the lower limit of 6.4 A/phase for the linear regression effects-based method deployed in [19] for a smaller transformer. It is noteworthy that the risk of power transformer overheating is insignificant for both lower detection thresholds [29]. IEEE Standard C57.163 classifies transformers with GIC magnitudes lower than 15 A/phase as having low GIC exposure [33]. Transformers with low GIC exposure may still be subjected to vibrations and accelerated winding insulation degradation that can cause failures over the long run [34], [35], but these low exposure effects remain insignificant below 1 A/phase. The authors did not find any literature that suggests that GIC magnitudes below 1 A/phase can cause negative consequences for transmission-level power transformers. Therefore, the lower detection threshold of the proposed method is sufficient to capture any crucial GIC effects that may occur in the bulk power system.

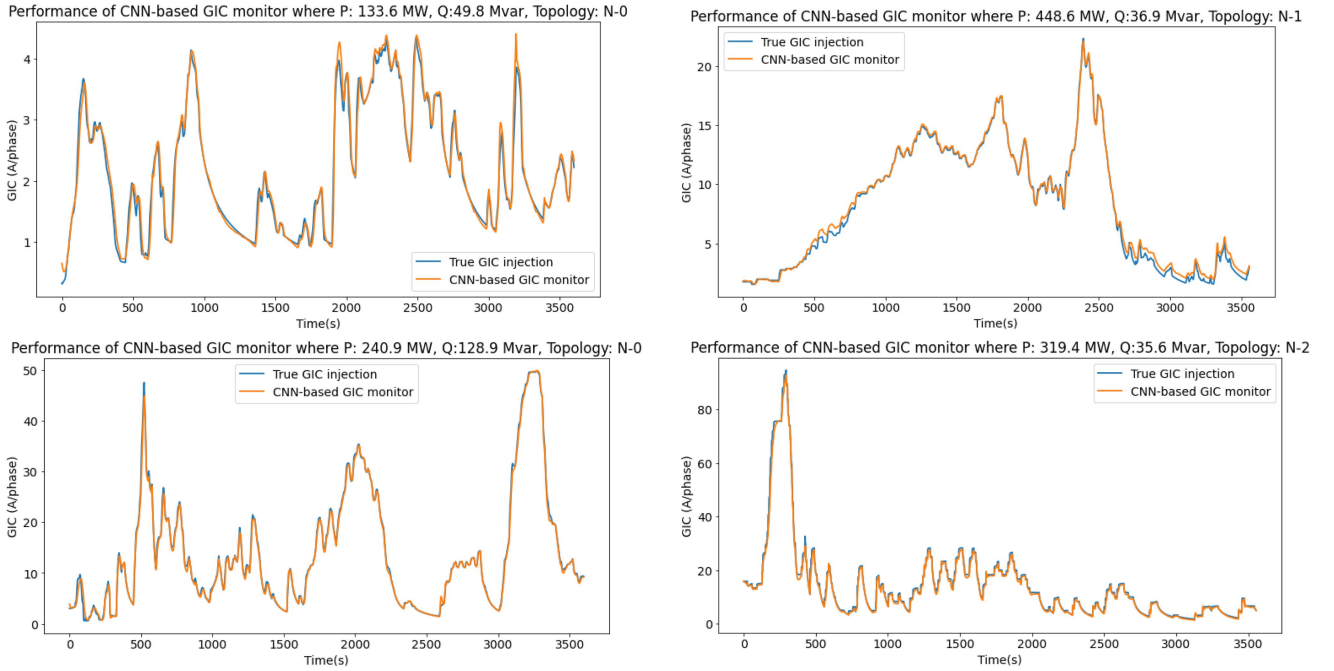


Fig. 10. Comparison of CNN-based GIC monitor output with true GIC injection at the transformer neutral for different operating conditions.

Previous works that used linear regression effects-based method provided no statistical information about the accuracy of their linear models [19]. Hence, an attempt was made to reenact their work by creating a linear regressor based on the relationship between 2-LV, 2-HV, and GIC. Neither oscillating GIC nor time-series harmonic values were considered in their work, therefore the linear regressor was created using the final steady-state values of the harmonics for constant magnitude GICs in the training dataset. Eq. (3) shows the equation of the linear regressor. Note that the coefficients in (3) are peculiar to the simulated transformers in this work.

$$I_{gic} = 1.3416 \cdot 2^{HV} + 1.2947 \cdot 2^{LV} + 2.4622 \quad (3)$$

Where  $2^{HV}$  and  $2^{LV}$  are the final steady-state values of the 2<sup>nd</sup> harmonic current induced by  $I_{gic}$  at the transformer primary and secondary sides.

The  $R^2$  coefficient of determination of the linear model was 0.994, showing the strong linear relationship between the model parameters. However, when this linear model was used to compute  $I_{gic}(t)$  against  $2^{HV}(t)$  and  $2^{LV}(t)$  in the test dataset, its RMSE and ANZG were 7.09 A/phase and 63.3% respectively. This performance is considerably lower than the performance of the proposed method. Moreover, to capture temporal dependencies between GIC and harmonics, another linear model was created using all the data available to the CNN including the time-series data of all three harmonic orders, along with  $P$ ,  $Q$ , and  $tp$  as shown in (4).

$$I_{gic}(t) = a_0 + a_1 \cdot n^{HV}(t) + \dots + a_{270} \cdot n^{LV}(t - 44) + a_{271} \cdot P(t) + a_{272} \cdot Q(t) + a_{273} \cdot tp \quad (4)$$

$n = 2, 4, \text{ and } 6$

TABLE III  
PERFORMANCE OF CNN FOR UNFAMILIAR NETWORK TOPOLOGIES

		RMSE (A/phase) on test topology [4NZG]		
		N-0	N-1	N-2
Training topology	N-0	<b>1.73 [91.8%]</b>	2.94 [86.6%]	3.06 [84.7%]
	N-1	3.08 [85.9%]	<b>1.58 [92.6%]</b>	1.59 [90.6%]
	N-2	4.83 [81.4%]	1.52 [92.2%]	<b>1.52 [92.6%]</b>

The coefficients,  $a_1$  to  $a_{273}$ , and intercept,  $a_0$ , were determined using the linear regression model in Python's scikit learn library. The  $R^2$  coefficient of this model was also high at 0.932, but RMSE and ANZG over the test data were 2.71 A/phase and 58.5% respectively. This RMSE is better than the previous linear model, but accuracy is worse. This suggests that the performance of this model is skewed towards larger GIC amplitudes. Nonetheless, the proposed method using a CNN still considerably outperforms both models because it captures both temporal and non-linear dependencies between GIC and harmonics.

### B. CNN Performance Over Unfamiliar Network Topology

Network topology influences system impedance, hence, it affects harmonic levels due to GIC (see Fig. 7). However, it is difficult to account for all possible network topologies in the simulations. Therefore, this subsection evaluates the performance of the CNN for unfamiliar network topologies. To achieve this, the CNN was trained only on the training data for one topology, then it is tested on the test data of the other two topologies. Table III presents the best performance of the 1-topology CNNs over multiple training runs. Note that the CNN

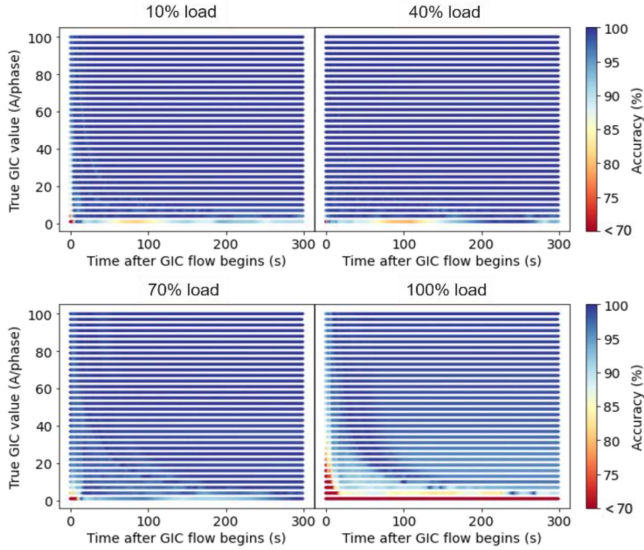


Fig. 11. Detection speed for different GIC amplitudes and transformer load levels.

hyperparameters were not re-tuned for the 1-topology dataset. So, the main inference from Table III should be the change in performance of the 1-topology CNN when evaluated on test data from other topologies compared to test data from its training topology.

The performance of the 1-topology CNNs in Table III suggests that the proposed method can still be useful to detect GIC for unknown network topologies, albeit with less accuracy. Accuracy drop is minimal when the CNN was trained on N-1 topology data and tested on N-2 data and vice versa. This is because system impedances for these two topologies are closer to each other than they are to system impedance at N-0 topology (see Table I). It is therefore recommended to train the CNN with data for a few representative (or common) network topologies. Then, the CNN can provide approximate GIC readings for other unfamiliar network topologies.

### C. GIC Detection Speed

An important consideration that was not explored in previous literature on effects-based GIC monitoring is the speed of accurate detection after GIC injection begins [19], [20]. Early detection will allow system operators to take fast actions to mitigate GIC impacts, and redispatch load away from affected transformers, thereby preserving power quality and elongating transformer fatigue life. Of course, the latency of data transfer and data processing will delay the detection speed of any effects-based GIC monitor. Assuming data transfer and processing times are negligible, the detection speed was evaluated by injecting different levels of constant magnitude GIC into the transformer for four load levels. These load levels were approximately 10%, 40%, 70%, and 100% of the transformer nameplate capacity and were not in the training dataset. Fig. 11 shows the detection speed of the CNN when different GIC amplitudes (1 – 100 A/phase in steps of 3 A) were injected at the load levels.

TABLE IV  
CNN PERFORMANCE WITH AND WITHOUT  $\Delta Q_{gic}$  DATA INPUT

	CNN with harmonic inputs	CNN with harmonic inputs + $\Delta Q_{gic}$
RMSE on test data (A/phase)	1.56	1.63
ANZG on test data (%)	94.1%	95.4%

Detection speed was generally fast when high GIC amplitudes were injected across all load levels. However, lower GIC amplitudes were slower to detect especially at larger transformer loads where harmonic damping is typically higher. It is reasonable that the detection speed would be dependent on GIC magnitude and transformer loading since harmonic generation is caused by transformer saturation, and the quickness of saturation depends on GIC magnitude and transformer loading [36], [37]. Nevertheless, it can be argued that higher GIC amplitudes where accurate detection is generally faster are of more interest to system operators than low GIC amplitudes, thus, the proposed method remains useful for GIC monitoring.

### D. Sensitivity Analysis: Addition of GIC-Induced Reactive Power Consumption to CNN Input Features

Besides harmonics,  $\Delta Q$  is also an important indicator of transformer saturation due to GIC [31]. Therefore, this section investigates potential performance improvements if time-series data of  $\Delta Q$  are added to the input features of the CNN. It is worth mentioning that the use of  $\Delta Q$  as an input may increase the chances of false positives. This is because an increase in  $\Delta Q$  can be caused by factors besides GIC, e.g., voltage change at either side of the transformer. Ref [18] isolated GIC-induced  $\Delta Q$  ( $\Delta Q_{gic}$ ) by finding the difference between measured  $\Delta Q$  and state estimated  $\Delta Q$  while accounting for normal calibration errors between the two values. However, sufficient data is not always available to calculate a representative calibration error between state estimation and measured values for all operating conditions. Nevertheless, time-series data of  $\Delta Q_{gic}$  was added to the CNN input with an optimistic assumption that highly accurate state estimation exists, or calibration error is known with high certainty.  $\Delta Q_{gic}(t)$  is calculated as the difference between  $\Delta Q(t)$  and  $\Delta Q_0$  before GIC injection began.

The result of the sensitivity analysis is presented in Table IV which shows that the addition of  $\Delta Q_{gic}$  does not improve the performance of the CNN. This is because  $\Delta Q_{gic}$  has a similar temporal relationship with GIC as harmonics (see Fig. 1), therefore, it does not add significant new information as an input to the CNN. Thus, the addition of  $\Delta Q_{gic}$  data to the CNN input is not recommended considering the discussed complications surrounding its use.

## V. CONCLUSION

This work explores the use of a convolutional neural network to provide an effects-based monitor for GIC in the neutral of a transformer. The CNN was utilized to recognize the trajectories of the 2<sup>nd</sup>, 4<sup>th</sup>, and 6<sup>th</sup> transformer current harmonics in order

to quantify GIC amplitudes at a given time. Other parameters such as transformer loading and topology information were also provided as inputs to the CNN. After training the CNN, it was tested against various GIC signals created by scaling real GIC measurements from DEV and published literature. The CNN provided readings with a root mean squared error of 1.56 A/phase (or 94% average accuracy) relative to the GIC signals for unfamiliar transformer operating conditions. It was further revealed that the CNN provided useful estimates of GIC when tested on data from network topologies that it was not trained for. The estimation accuracy however depends on the difference in system impedance between the topologies included in the CNN training and the ones it is tested on. Furthermore, four transformer loading scenarios were used to show that the GIC detection speed of the CNN is dependent on GIC magnitudes and transformer loading. Finally, a sensitivity analysis showed that the addition of reactive power consumption as an input does not significantly improve the performance of the CNN for GIC monitoring.

Like other effects-based GIC methods, the proposed method will have to be implemented for individual substations or transformers. Future work would explore the potentials of transfer learning to reuse learned CNN weights at one substation for other substations.

#### ACKNOWLEDGMENT

Special thanks to ET Operations Team, Dominion Energy Virginia for sponsorship and provision of data and expertise for this research.

#### REFERENCES

- [1] H. Root, "Earth-current effects on communication-cable power subsystems," *IEEE Trans. Electromagn. Compat.*, vol. EMC-21, no. 2, pp. 87–92, May 1979, doi: [10.1109/temc.1979.303750](https://doi.org/10.1109/temc.1979.303750).
- [2] W. H. Campbell, "Observation of electric currents in the Alaska oil pipeline resulting from auroral electrojet current sources," *Geophys. J. Int.*, vol. 61, no. 2, pp. 437–449, May 1980, doi: [10.1111/j.1365-246x.1980.tb04325.x](https://doi.org/10.1111/j.1365-246x.1980.tb04325.x).
- [3] B. Efimov, V. Selivanov, and Y. Sakharov, "Impact of geomagnetically induced currents on transformers in the kola power grid," in *Proc. Int. Multi-Conf. Ind. Eng. Modern Technol. (FarEastCon)*, 2019, pp.1–4, doi: [10.1109/fareastcon.2019.8933828](https://doi.org/10.1109/fareastcon.2019.8933828).
- [4] R. A. Walling and A. N. Khan, "Characteristics of transformer exciting-current during geomagnetic disturbances," *IEEE Trans. Power Del.*, vol. 6, no. 4, pp. 1707–1714, Oct. 1991, doi: [10.1109/61.977710](https://doi.org/10.1109/61.977710).
- [5] S. Adhikari, D. Mueller, R. Walling, and A. J. O'Laughlin, "A comprehensive study of geomagnetic disturbance (GMD) system impact," in *Proc. IEEE Power Energy Soc. Gen. Meeting*, 2017, pp.1–5, doi: [10.1109/pesgm.2017.8273848](https://doi.org/10.1109/pesgm.2017.8273848).
- [6] Z. M. K. Abda, N. F. A. Aziz, M. Z. A. A. Kadir, and Z. A. Rhazali, "A review of geomagnetically induced current effects on electrical power system: Principles and theory," *IEEE Access*, vol. 8, pp. 200237–200258, 2020, doi: [10.1109/access.2020.3034347](https://doi.org/10.1109/access.2020.3034347).
- [7] S. Guillon, P. Toner, L. Gibson, and D. Boteler, "A colorful blackout: The havoc caused by auroral electrojet generated magnetic field variations in 1989," *IEEE Power Energy Mag.*, vol. 14, no. 6, pp. 59–71, Nov./Dec. 2016, doi: [10.1109/mpe.2016.2591760](https://doi.org/10.1109/mpe.2016.2591760).
- [8] M. Wik, R. Pirjola, H. Lundstedt, A. Viljanen, P. Wintoft, and A. Pulkkinen, "Space weather events in July 1982 and October 2003 and the effects of geomagnetically induced currents on Swedish technical systems," *Annales Geophysicae*, vol. 27, no. 4, pp. 1775–1787, Apr. 2009, doi: [10.5194/angeo-27-1775-2009](https://doi.org/10.5194/angeo-27-1775-2009).
- [9] R. Sun, M. Mcvey, M. Lamb, and R. M. Gardner, "Mitigating geomagnetic disturbances: A summary of dominion virginia Power's efforts," *IEEE Electrific. Mag.*, vol. 3, no. 4, pp. 34–45, Dec. 2015, doi: [10.1109/mele.2015.2480636](https://doi.org/10.1109/mele.2015.2480636).
- [10] C. T. Gaunt and G. Coetzee, "Transformer failures in regions incorrectly considered to have low GIC-risk," in *Proc. IEEE Lausanne Power Tech*, 2007, pp. 807–812, doi: [10.1109/pct.2007.4538419](https://doi.org/10.1109/pct.2007.4538419).
- [11] J. Beland and K. Small, "Space weather effects on power transmission systems: The cases of hydro-québec and transpower New Zealand Ltd.," In: I. A. Daglis, (eds.) *Effects of Space Weather On Technological Infrastructure*, NATO Science Series II: Mathematics, Physics and Chemistry, Netherlands: Kluwer Academic Publishers, 2004, ch. 15, pp. 287–299.
- [12] M. Nazir, K. Burkes, and J. H. Enslin, "Electrical safety considerations of neutral blocker placements for mitigating DC," *IEEE Trans. Ind. Appl.*, vol. 57, no. 1, pp. 1113–1121, Jan./Feb. 2021, doi: [10.1109/tia.2020.3032081](https://doi.org/10.1109/tia.2020.3032081).
- [13] M. A. Clilverd *et al.*, "Geomagnetically induced currents and harmonic distortion: High time resolution case studies," *Space Weather*, vol. 18, no. 10, Oct. 2020, Art. no. e2020SW002594, doi: [10.1029/2020sw002594](https://doi.org/10.1029/2020sw002594).
- [14] D. H. Mac Manus *et al.*, "Long-term geomagnetically induced current observations in New Zealand: Earth return corrections and geomagnetic field driver," *Space Weather*, vol. 15, no. 8, pp. 1020–1038, Aug. 2017, doi: [10.1002/2017sw001635](https://doi.org/10.1002/2017sw001635).
- [15] C. Klauber, K. Shetye, T. J. Overbye, and K. Davis, "A GIC estimator for electric grid monitoring during geomagnetic disturbances," *IEEE Trans. Power Syst.*, vol. 35, no. 6, pp. 4847–4855, Nov. 2020, doi: [10.1109/tpwrs.2020.3000746](https://doi.org/10.1109/tpwrs.2020.3000746).
- [16] S. Watari, "Estimation of geomagnetically induced currents based on the measurement data of a transformer in a Japanese power network and geoelectric field observations," *Earth, Planets Space*, vol. 67, no. 1, 2015, Art. no. 77, doi: [10.1186/s40623-015-0253-8](https://doi.org/10.1186/s40623-015-0253-8).
- [17] D. H. Boteler *et al.*, "Real-time simulation of geomagnetically induced currents," in *Proc. 7th Int. Symp. Electromagn. Compat. Electromagn. Ecol.*, 2007, pp. 261–264, doi: [10.1109/emceco.2007.4371705](https://doi.org/10.1109/emceco.2007.4371705).
- [18] L. Marti, J. Berge, and R. K. Varma, "Determination of geomagnetically induced current flow in a transformer from reactive power absorption," *IEEE Trans. Power Del.*, vol. 28, no. 3, pp. 1280–1288, Jul. 2013, doi: [10.1109/tpwr.2012.2219885](https://doi.org/10.1109/tpwr.2012.2219885).
- [19] E. E. Bernabeu, "Single-Phase transformer harmonics produced during geomagnetic disturbances: Theory, modeling, and monitoring," *IEEE Trans. Power Del.*, vol. 30, no. 3, pp. 1323–1330, Jun. 2015, doi: [10.1109/tpwr.2014.2371927](https://doi.org/10.1109/tpwr.2014.2371927).
- [20] S. Wang, P. Dehghanian, L. Li, and B. Wang, "A machine learning approach to detection of geomagnetically induced currents in power grids," *IEEE Trans. Ind. Appl.*, vol. 56, no. 2, pp. 1098–1106, Mar./Apr. 2020, doi: [10.1109/tia.2019.2957471](https://doi.org/10.1109/tia.2019.2957471).
- [21] L. Bolduc, A. Gaudreau, and A. Dutil, "Saturation time of transformers under dc excitation," *Electric Power Syst. Res.*, vol. 56, no. 2, pp. 95–102, Nov. 2000, doi: [10.1016/s0378-7796\(00\)00087-0](https://doi.org/10.1016/s0378-7796(00)00087-0).
- [22] H. Ismail Fawaz, G. Forestier, J. Weber, L. Idoumghar, and P.-A. Muller, "Deep learning for time series classification: A review," *Data Mining Knowl. Discov.*, vol. 33, no. 4, pp. 917–963, 2019, doi: [10.1007/s10618-019-00619-1](https://doi.org/10.1007/s10618-019-00619-1).
- [23] Z. Wang, W. Yan, and T. Oates, "Time series classification from scratch with deep neural networks: A strong baseline," in *Proc. Int. Joint Conf. Neural Netw.*, 2017, pp. 1578–1585, doi: [10.1109/ijcnn.2017.7966039](https://doi.org/10.1109/ijcnn.2017.7966039).
- [24] N. Strodthoff and C. Strodthoff, "Detecting and interpreting myocardial infarction using fully convolutional neural networks," *Physiol. Meas.*, vol. 40, no. 1, 2019, Art. no. 015001, doi: [10.1088/1361-6579](https://doi.org/10.1088/1361-6579).
- [25] A. Haddadi, R. Hassani, J. Mahseredjian, L. Gerin-Lajoie, and A. Rezaei-Zare, "Evaluation of simulation methods for analysis of geomagnetic disturbance system impacts," *IEEE Trans. Power Del.*, vol. 36, no. 3, pp. 1509–1516, Jun. 2021, doi: [10.1109/tpwr.2020.3010195](https://doi.org/10.1109/tpwr.2020.3010195).
- [26] PSCAD "PSCAD knowledge base: Transformer saturation curve matching in PSCAD™/EMTDC™," Accessed: Jul. 13, 2021. [Online]. Available: <https://www.pscad.com/knowledge-base/article/561>
- [27] PSCAD, *PSCAD Knowledge Base: Applications of PSCAD/EMTDC*, 2008. Accessed: Jul. 13, 2021. [Online]. Available: [https://www.pscad.com/knowledge-base/download/application\\_20guide\\_202008\\_1.pdf](https://www.pscad.com/knowledge-base/download/application_20guide_202008_1.pdf)
- [28] E. E. Bernabeu, "Modeling geomagnetically induced currents in dominion virginia power using extreme 100-Year geoelectric field scenarios—Part 1," *IEEE Trans. Power Del.*, vol. 28, no. 1, pp. 516–523, Jan. 2013, doi: [10.1109/tpwr.2012.2224141](https://doi.org/10.1109/tpwr.2012.2224141).

- [29] NERC, "Transformer thermal impact assessment white paper: TPL-007-2 – transmission system planned performance for geomagnetic disturbance events." [Online]. Available: [https://www.nerc.com/pa/Stand/Project201303GeomagneticDisturbanceMitigation/Thermal\\_Impact\\_Assessment\\_2017\\_October\\_Clean.pdf](https://www.nerc.com/pa/Stand/Project201303GeomagneticDisturbanceMitigation/Thermal_Impact_Assessment_2017_October_Clean.pdf)
- [30] V. N. Rajput, D. H. Boteler, N. Rana, M. Saiyed, S. Anjana, and M. Shah, "Insight into impact of geomagnetically induced currents on power systems: Overview, challenges and mitigation," *Electric Power Syst. Res.*, vol. 192, Mar. 2021, Art. no. 106927, doi: [10.1016/j.epsr.2020.106927](https://doi.org/10.1016/j.epsr.2020.106927).
- [31] X. Dong, Y. Liu, and J. G. Kappenman, "Comparative analysis of exciting current harmonics and reactive power consumption from GIC saturated transformers," in *Proc. IEEE Power Eng. Soc. Winter Meeting. Conf. Proc. (Cat. No.01CH37194)*, 2001, pp. 318–322, doi: [10.1109/pesw.2001.917055](https://doi.org/10.1109/pesw.2001.917055).
- [32] I. Goodfellow, Y. Bengio, and A. Courville, "Convolutional networks," in *Deep Learning*. Cambridge, MA, USA: MIT Press, 2016, pp. 326–366.
- [33] *IEEE Guide for Establishing Power Transformer Capability while under Geomagnetic Disturbances*, IEEE Standard C57.163-2015, Oct. 2015, doi: [10.1109/ieeestd.2015.7286929](https://doi.org/10.1109/ieeestd.2015.7286929).
- [34] C. A. Baguley, U. K. Madawala, and B. Carsten, "The impact of vibration due to magnetostriction on the core losses of ferrite toroidals under DC bias," *IEEE Trans. Magn.*, vol. 47, no. 8, pp. 2022–2028, Aug. 2011, doi: [10.1109/tmag.2011.2129523](https://doi.org/10.1109/tmag.2011.2129523).
- [35] EPRI, "3002017707 – assessment guide: Geomagnetic disturbance harmonic impacts and asset withstand capabilities," Tech. Update. [Online]. Available: <https://www.epri.com/research/products/000000003002017707>
- [36] A. A. Ademola, X. Li, D. Yang, and M. J. Till, "Comparative study of the reactive power consumption of a dominion energy Virginia autotransformer due to geomagnetically-induced current," in *Grid of the Future Symposium*, J. D. McDonald, Ed., Providence, RI, USA: CIGRE U.S. National Committee, 2021.
- [37] A. P. S. Meliopoulos, E. N. Glytsis, G. J. Cokkinides, and M. Rabinowitz, "Comparison of SS-GIC and MHD-EMP-GIC effects on power systems," *IEEE Trans. Power Del.*, vol. 9, no. 1, pp. 194–207, Jan. 1994, doi: [10.1109/61.277691](https://doi.org/10.1109/61.277691).